Available online at www.sciencedirect.com

SciVerse ScienceDirect

Procedia Computer Science 9 (2012) 832 – 841

Procedia Computer Science

www.elsevier.com/locate/procedia

International Conference on Computational Science, ICCS 2012

Scaling Properties of Multi-Fidelity Shape Optimization Algorithms

Slawomir Koziel[a], Leifur Leifsson[a*]

[a]*Engineering Optimization & Modeling Center, School of Science and Engineering, Reykjavik University, Menntavegur 1, 101 Reykjavik, Iceland*

Abstract

Multi-fidelity optimization can be utilized for efficient design of airfoil shapes. In this paper, we investigate the scaling properties of algorithms exploiting this methodology. In particular, we study the relationship between the computational cost and the size of the design space. We focus on a specific optimization technique where, in order to reduce the design cost, the accurate high-fidelity airfoil model is replaced by a cheap surrogate constructed from a low-fidelity model and the shape-preserving response prediction technique. In this study, we consider the design of transonic airfoils and use the compressible Euler equations in the high-fidelity computational fluid dynamic (CFD) model. The low-fidelity CFD model is same as the high-fidelity one, but with coarser mesh resolution and reduced level of solver converge. The number of design variables varies from 3 to 11 by using NACA 4-digit airfoil shapes as well as airfoils constructed by Bézier curves. The results of the three optimization studies show that total cost increases from about 12 equivalent high-fidelity model evaluations to 34. The number of high-fidelity evaluations increases from 4 to 9, whereas the number of low-fidelity evaluations increases more rapidly, from 600 to 2000. This indicates that, while the overall optimization cost scales more or less linearly with the dimensionality of the design space, further cost reduction can be obtained through more efficient optimization of the surrogate model.

Keywords: curse of dimensionality; algorithm scalability; multi-fidelity optimization; aerodynamic design; CFD; physics-based surrogates.

1. Introduction

Surrogate-based optimization (SBO) [1-3] is the basis of many efficient aerodynamic design techniques, see, e.g., [4-6]. Many conventional SBO techniques construct the surrogate by approximating the sampled high-fidelity simulations data, estimate the optimum design based on the surrogate, and then validate the optimum by performing a high-fidelity simulation. This cycle is repeated until convergence or until a satisfactory design is found. For a given set of design variables, the overall computational cost of SBO compared to conventional direct optimization approaches, such as gradient-based or population-based methods, may be significantly lower. However, the conventional SBO is still limited by the *curse of dimensionality*, i.e., the computational cost increases rapidly with the size of the design space.

The surrogate model construction is typically realized in five steps: (1) selection of the design variables, (2) sampling of the design space, often called design of experiments (DOE), (3) acquisition of high-fidelity model data, (4) model identification, and, finally, (5) model validation [2]. Numerous methods for sampling the design space are available, including factorial design or Latin hypercube sampling [1]. In general, the number of samples required by

* Corresponding author. Tel.: +354-599-6200 ; Fax: +354-599-6201; *E-mail address*: leifurth@ru.is

doi:10.1016/j.procs.2012.04.089

such methods increases exponentially with the dimension of the design space [2]. One way of addressing this is by reducing the dimensionality of the problem. This can be achieved using methods such as treed meta-model (TMM) framework [7], and generative topographic mapping [8]. This, however, only partially alleviates the problem.

Another way of constructing the surrogate is by low-fidelity modeling – called multi- or variable-fidelity modeling [4-6]. Here, the low-fidelity model can be, for example, a simplified physics model, a computational fluid dynamics (CFD) model of different mesh resolution, a CFD model with a different level of convergence, or a combination of the aforementioned models. The fundamental difference of this approach compared to the functional surrogate modeling approach is that the knowledge about the physical system of interest is embedded in the low-fidelity model. This allows us to obtain a relatively accurate surrogate model with good generalization properties using a very low amount of high-fidelity model data (in some cases, a single high-fidelity model sample may be sufficient). Typically, the surrogate is created by means of suitable manipulation of the low-fidelity model domain (e.g., space mapping, SM [9]) or a proper response correction technique, e.g., shape-preserving response prediction (SPRP) [6]. The potential disadvantage of multi-fidelity techniques is that low-fidelity model may be relatively expensive. Nevertheless, multi-fidelity shape optimization seems to offer significant reduction of the overall optimization cost, see, e.g., [5,6]. However, a study of the relationship between the cost and the number of design variables has not yet been reported in the literature for this kind of techniques.

In this work, the scaling properties of multi-fidelity airfoil shape optimization are investigated. We use variable-resolution modeling (varying levels of mesh density and solver convergence criteria) and the SPRP technique to construct the surrogate model. The airfoil shape is parameterized using two different techniques with the number of design variables ranging from three to eleven. One case study of airfoil optimization at transonic speeds is provided.

2. Multi-Fidelity Shape Optimization with SPRP

In this section, we describe the multi-fidelity airfoil shape optimization methodology. We focus on a specific design approach that exploits shape-preserving response prediction (SPRP) technique [6]. We discuss the problem formulation, the optimization algorithm, as well as surrogate modeling through SPRP.

2.1. Problem Formulation

Airfoil shape optimization can be formulated as a constrained nonlinear minimization problem, i.e., for a given operating condition, solve

$$\min_{\boldsymbol{x}} f(\boldsymbol{x}) \; s.t. \; g_j(\boldsymbol{x}) \le 0, \; j = 1,\ldots,M, h_k(\boldsymbol{x}) = 0, \; k = 1,\ldots,N, \; \boldsymbol{l} \le \boldsymbol{x} \le \boldsymbol{u}, \tag{1}$$

where $f(\boldsymbol{x})$ is the objective function, $\boldsymbol{x}$ is the design variable vector (details of the airfoil parameterization methods used in this work are given in Section 3), $g_j(\boldsymbol{x})$ are the inequality constraints, M is the number of the inequality constraints, $h_k(\boldsymbol{x})$ are the equality constraints, N is the number of the equality constraints, and $\boldsymbol{l}$ and $\boldsymbol{u}$ are the design variables lower and upper bounds, respectively. The detailed formulation then depends on the particular design scenario. In this work, we consider lift maximization with the following formulation: for a given operating condition of Mach number M_∞ and an angle of attack α, minimize the negative section lift coefficient, $f(\boldsymbol{x}) = -C_l(\boldsymbol{x})$, subject to constraints on the section drag coefficient, $g_1(\boldsymbol{x}) = C_{dw}(\boldsymbol{x}) - C_{dw}^{desired} \le 0$, and the cross-sectional area, $g_2(\boldsymbol{x}) = A_{min} - A(\boldsymbol{x}) \le 0$.

Due to unavoidable misalignment between the pressure distributions of the high-fidelity model and its SPRP surrogate, it is not convenient to handle the drag constraint directly, because the design that is feasible for the surrogate model, may not be feasible for the high-fidelity model. In particular, the design obtained as a result of optimizing the surrogate model $C_{p.s}^{(i)}$, i.e., $\boldsymbol{x}^{(i+1)}$, will be feasible for $C_{p.s}^{(i)}$. However, if $\boldsymbol{x}^{(i+1)}$ is not feasible for the high-fidelity model, it will not be feasible for $C_{p.s}^{(i+1)}$ because we have $C_{p.s}^{(i+1)}(\boldsymbol{x}^{(i+1)}) = C_{p.f}(\boldsymbol{x}^{(i+1)})$ by the definition of the surrogate model. In order to alleviate this problem, the constraints are implemented through penalty functions.

More specifically, the objective function is defined as

$$H(C_p(\boldsymbol{x})) = -C_{l.s}(C_p(\boldsymbol{x})) + \beta\left[\Delta C_{dw.s}(C_p(\boldsymbol{x}))\right]^2, \tag{2}$$

where $\Delta C_{dw.s} = 0$ if $C_{dw.s} \le C_{dw.s.max}$ and $\Delta C_{dw.s} = C_{dw.s} - C_{dw.s.max}$ otherwise. The cross-sectional area constraint is handled directly. We use $\beta = 1000$ in our numerical studies. Here, the pressure distribution for the surrogate model

is $C_p = C_{p.s}$, and for the high-fidelity model $C_p = C_{p.f}$. Also, $C_{l.s}$ and $C_{dw.s}$ denote the lift and wave drag coefficients (both being functions of the pressure distribution).

2.2. Optimization Algorithm

The airfoil design process is accelerated by using surrogate-based optimization (SBO) [1-3] with physics-based low-fidelity models. The low-fidelity model inherits knowledge about the system under consideration (here, the airfoil) and can be used to create a fast and yet accurate representation of the high-fidelity model, a surrogate. The surrogate model is then used as a prediction tool that yields an approximate high-fidelity model optimum at a low computational cost [10]. The flow diagram of the SBO process exploiting SPRP surrogate model is shown in Fig. 1. In next section, we describe the process of creating the surrogate model s using a specific approach – shape-preserving response prediction (SPRP) [6,11]. The details of the high- and low-fidelity models used in this work are given in Section 4.

2.3. Surrogate Modeling with SPRP

A shape-preserving response prediction (SPRP) methodology was initially introduced in [11] in the context of microwave engineering. SPRP is easy to implement and it does not use any explicit parameters that need to be extracted [11]. Also, SPRP does not require high-fidelity model derivative information. The main components of the surrogate are: the low-fidelity CFD model, the data obtained from a single high-fidelity CFD model evaluation, and a response prediction technique. Figure 1 shows the overall process of the surrogate model construction using SPRP.

By formulation, SPRP works directly with the model outputs that can be described by certain number of design-variable-dependent characteristic features [11]. In the case of a pressure distribution, these features may include the location and strength of the shock, the pressure at the leading- and trailing-edges, and many others. In direct airfoil design, the pressure distribution is an intermediate simulation result, with the figures of interest, such as lift or drag, being derived from it. In inverse design, the pressure distribution is the main object of interest, which makes SPRP well suited for this kind of problem.

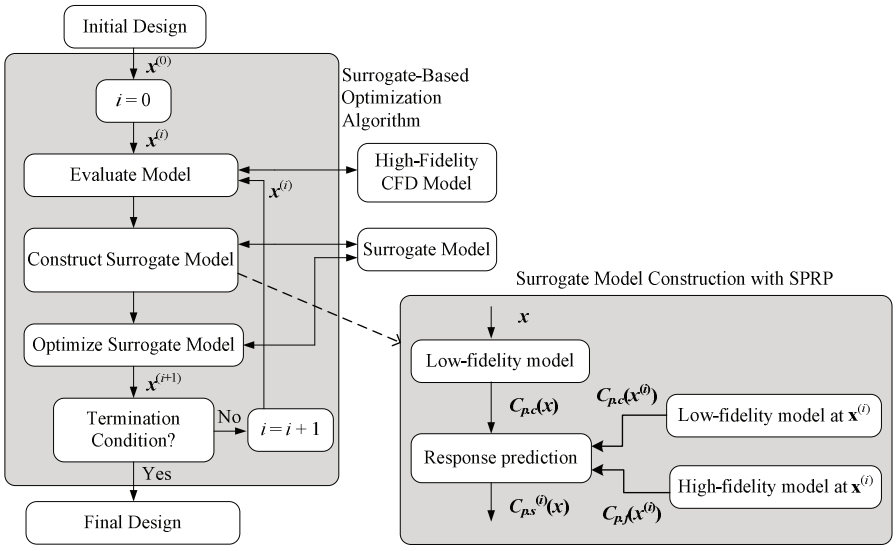

Fig. 1. The flow of the surrogate-based optimization (SBO) algorithm and the details of the surrogate model construction at design iteration i using shape-preserving response prediction (SPRP). The high-fidelity pressure distribution at a design $\boldsymbol{x}$, the surrogate $C_{p.s}(\boldsymbol{x})$, is predicted using the high-fidelity model data at a reference design $\boldsymbol{x}^{(i)}$, $C_{p.f}(\boldsymbol{x}^{(i)})$, and the change of the low-fidelity pressure distribution from $\boldsymbol{x}^{(i)}$ to $\boldsymbol{x}$, $C_{p.c}(\boldsymbol{x}^{(i)})$ and $C_{p.c}(\boldsymbol{x})$, respectively.

The pressure distribution for the high- and low-fidelity models will be denoted as $C_{p.f}$ and $C_{p.c}$, respectively. The surrogate model is constructed assuming that the change of $C_{p.f}$ due to the adjustment of the design variables $\boldsymbol{x}$ can be predicted using the actual changes of $C_{p.c}$. The change of $C_{p.c}$ is described by the translation vectors corresponding to certain (finite) number of its characteristic points. These translation vectors are subsequently used to predict the change of $C_{p.f}$, whereas the actual $C_{p.f}$ at the current design, $C_{p.f}(\boldsymbol{x}^{(i)})$, is treated as a reference.

Figure 2a shows the pressure distribution $C_{p.c}$ of the low-fidelity model at $\boldsymbol{x}^{(i)} = [m\ p\ t/c]^T = [0.02\ 0.4\ 0.12]^T$ (NACA 2412 airfoil) for $M_\infty = 0.7$ and $\alpha = 1°$, as well as $C_{p.c}$ at $\boldsymbol{x} = [0.025\ 0.56\ 0.122]^T$; $\boldsymbol{x}^{(i)}$ will denote a current design (at the ith iteration of the optimization algorithm; the initial design will be denoted as $\boldsymbol{x}^{(0)}$ accordingly). Circles denote characteristic points of $C_{p.c}(\boldsymbol{x}^{(i)})$, here, representing, among others, x/c equal to 0 and 1 (leading and trailing airfoil edges, respectively), the maxima of $C_{p.c}$ for the lower and upper airfoil surfaces, as well as the local minimum of $C_{p.c}$ for the upper surface. The last two points are useful to locate the pressure shock. Squares denote corresponding characteristic points for $C_{p.c}(\boldsymbol{x})$, while small line segments represent the translation vectors that determine the "shift" of the characteristic points of $C_{p.c}$ when changing the design variables from $\boldsymbol{x}^{(i)}$ to $\boldsymbol{x}$.

In order to obtain a reliable prediction, the number of characteristic points has to be larger than illustrated in Fig. 2a. Additional points are inserted in between initial points either uniformly with respect to x/c (for those parts of the pressure distribution that are almost flat) or based on the relative pressure value with respect to corresponding initial points (for those parts of the pressure distribution that are "steep"). Figure 2b shows the full set of characteristic points (initial points are distinguished using larger markers). The specific allocation of the additional characteristic points is not critical for the performance of the algorithm.

The pressure distribution of the high-fidelity model at the given design, here, $\boldsymbol{x}$, can be predicted using the translation vectors applied to the corresponding characteristic points of the pressure distribution of the high-fidelity model at $\boldsymbol{x}^{(i)}$, $C_{p.f}(\boldsymbol{x}^{(i)})$. This is illustrated in Fig. 3a, where only initial characteristic points and translation vectors are shown for clarity. Figure 3b shows the predicted pressure distribution of the high-fidelity model at $\boldsymbol{x}$ as well as the actual $C_{p.f}(\boldsymbol{x})$. The agreement between both curves is very good.

Rigorous formulation of the SPRP technique can be found in [11]. We omit the details here for the sake of brevity. It should be mentioned that the SPRP model assumes that the high- and low-fidelity model pressure distributions have corresponding sets of characteristic points. This is usually the case for the practical ranges of design variables because the overall shape of the distributions is similar for both models. In case of a lack of correspondence, original definitions of characteristic points are replaced by their closest counterparts. The typical example would be non-existence of the local minimum of the pressure distribution for the upper surface for the high- and/or low-fidelity model at certain designs. In this case, the original point (local minimum) is replaced by the points characterized by the largest curvature.

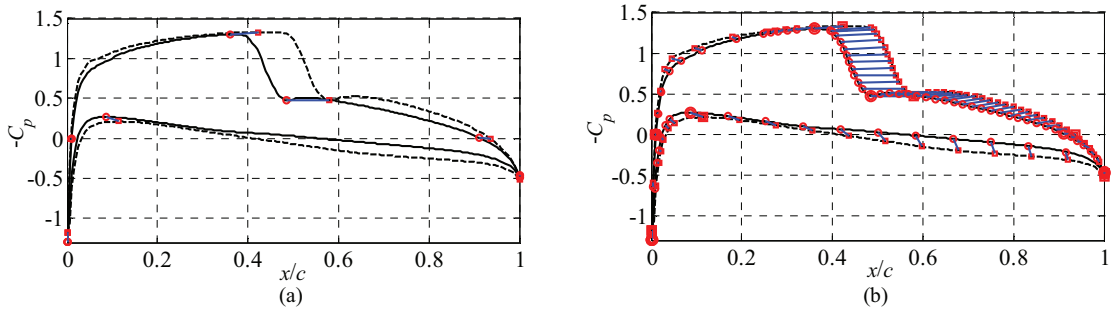

Fig. 2. (a) Example low-fidelity model pressure distribution at the design $\mathrm{x}^{(i)}$, $C_{p.c}(\mathrm{x}^{(i)})$ (solid line), the low-fidelity model pressure distribution at other design x, $C_{p.c}$(x) (dotted line), characteristic points of $C_{p.c}(\mathrm{x}^{(i)})$ (circles) and $C_{p.c}$(x) (squares), and the translation vectors (short lines); (b) low-fidelity model pressure distributions, initial characteristic points (large markers) and translation vectors from Fig. 2a as well as additional points (small markers) inserted in between the initial points either uniformly with respect to x/c (for those parts of the pressure distribution that are almost flat) or based on the relative pressure value with respect to corresponding initial points (for those parts of the pressure distribution that are "steep").

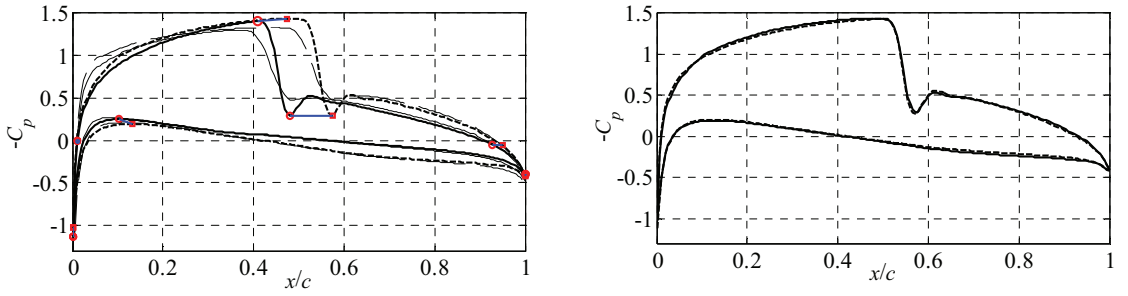

Fig. 3. (a) High-fidelity model pressure distribution at $x^{(i)}$, $C_{p,f}(x^{(i)})$ (solid line) and the predicted high-fidelity model C_p at x (dotted line) obtained using SPRP based on characteristic points of Fig. 2b; characteristic points of $C_{p,f}(x^{(i)})$ (circles) and the translation vectors (short lines) were used to find the characteristic points (squares) of the predicted high-fidelity model pressure distribution (only initial points are shown for clarity); low-fidelity model distributions $C_{p,c}(x^{(i)})$ and $C_{p,c}(x)$ are plotted using thin solid and dotted line, respectively; (b) high-fidelity model pressure distribution at x, $C_{p,f}(x)$ (solid line), and the predicted high-fidelity model pressure distribution at x obtained using SPRP (dotted line).

3. Airfoil Shape Parameterization

In this study, we apply the SPRP optimization technique to shape optimization of different sizes in order to investigate the relationship between the problem size and the computational cost of the optimization process. We use two different airfoil shape parameterization techniques. The NACA 4-digit airfoils [12] can be parameterized with only three design variables, but limited control is provided. Using Bézier curves [13] provides a better control of the shape. Here, we use Bézier curves to describe the airfoil shapes with seven and eleven design variables. The following is the description of these parameterization techniques.

3.1. NACA Airfoils

In the NACA four-digit parameterization method [12] the airfoil shape is defined by three parameters: m (the maximum ordinate of the mean camberline as a fraction of chord), p (the chordwise position of the maximum ordinate) and t/c (the maximum thickness-to-chord ratio). The airfoils are denoted as NACA $mpxx$, where xx is the maximum thickness-to-chord ratio, t/c. The design variable vector for this parameterization can be written as

$$\boldsymbol{x} = [m\ p\ t/c]^T. \tag{3}$$

The airfoils are constructed by combining a thickness function $z_t(x/c)$ with a mean camber line function $z_c(x/c)$. The x/c- and z/c-coordinates are [12]

$$(x/c)_{u,l} = (x/c) \mp (z_t/c)\sin\theta, \quad (z/c)_{u,l} = (z_c/c) \pm (z_t/c)\cos\theta \tag{4}$$

where u and l refer to the upper and lower surfaces, respectively, $z_t(x/c)$ is the thickness function, $z_c(x/c)$ is the mean camber line function, and

$$\theta = \tan^{-1}\left(\frac{d(z_c/c)}{d(x/c)}\right) \tag{5}$$

is the mean camber line slope. The NACA four-digit thickness distribution is given by

$$(z_t/c) = t(a_0(x/c)^{1/2} - a_1(x/c) - a_2(x/c)^2 + a_3(x/c)^3 - a_4(x/c)^4), \tag{6}$$

where $a_0 = 1.4845$, $a_1 = 0.6300$, $a_2 = 1.7580$, $a_3 = 1.4215$, $a_4 = 0.5075$, and t is the maximum thickness.

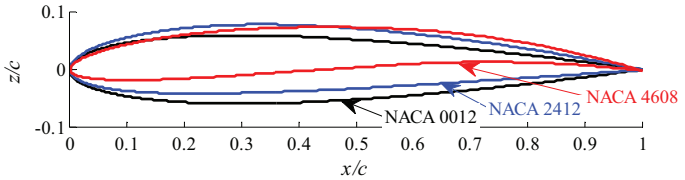

Fig. 4. Shown are three different NACA four-digit airfoil sections: NACA 0012 (m = 0, p = 0, t/c = 0.12), NACA 2412 (m = 0.02, p = 0.4, t/c = 0.12), and NACA 4608 (m = 0.04, p = 0.6, t/c = 0.08).

The mean camber line is given by

$$(z_c/c)=\frac{m}{p^2}(2p(x/c)-(x/c)^2)\,,\ (x/c)<p;\quad (z_c/c)=\frac{m}{(1-p)^2}(1-2p+2p(x/c)-(x/c)^2)\,,\ (x/c)\geq p\,. \quad (7)$$

Three example NACA four-digit airfoils are shown in Fig. 4.

3.2. Bézier Airfoils

Bézier curves [13] of order n are defined as

$$B(t)=\sum_{k=1}^{m}\sum_{i=0}^{n}\frac{n!}{i!(n-i)!}(1-b(k))^{n-i}b(k)^i P(i)\,, \quad (8)$$

where $P(i)$, i = 0,1,…n, are control points, and b is an 1 × m array with entries from 0 to 1. Any number of control points can be used to represent the airfoil shape. In this work, we use two setups, one with 6 control points and another with 8 control points. An example of these setups is shown in Fig. 5.

The setup with 6 control points, shown in Fig. 5a, is configured as follows. The control point at the leading-edge is fixed to the origin. There are two control points on the line x/c = 0, and two control points for the upper and lower surfaces. The control point at the trailing-edge is on the line x/c = 1. In total, this gives 7 shape parameters, and the design variable vector can be written as

$$\boldsymbol{x}=[(x/c)_u\ (x/c)_l\ (y/c)_{u,\mathrm{LE}}\ (y/c)_u\ (y/c)_{l,\mathrm{LE}}\ (y/c)_l\ (y/c)_{TE}]^T, \quad (9)$$

where u and l denote the upper and lower surfaces, LE is the leading-edge, and TE is the trailing-edge. The setup with 8 control points, shown in Fig. 5b, is identical, except that two free control points are added, one on the upper surface and the other on the lower surface. In this case, there are 11 shape parameters, and the design variable vector is

$$\boldsymbol{x}=[(x/c)_{u,1}\ (x/c)_{u,2}\ (x/c)_{l,1}\ (x/c)_{l,2}\ (y/c)_{u,\mathrm{LE}}\ (y/c)_{u,1}\ (y/c)_{u,2}\ (y/c)_{l,\mathrm{LE}}\ (y/c)_{l,1}\ (y/c)_{l,2}\ (y/c)_{TE}]^T, \quad (10)$$

where the numbers 1 and 2 refer to the free control points on the upper and lower surfaces.

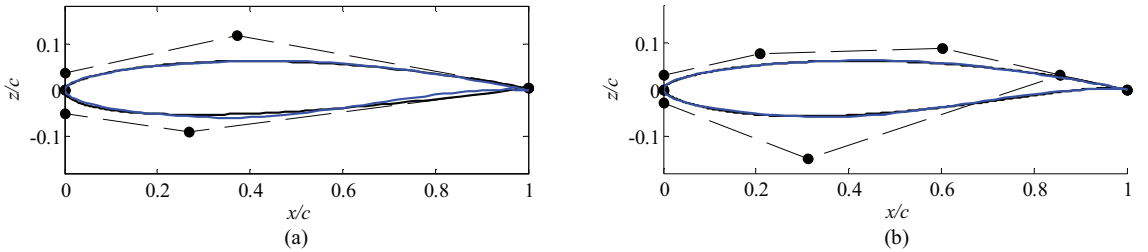

Fig. 5. Bézier curve approximations (solid black lines) of the RAE 2822 airfoil (solid blue lines); (a) with 6 control points and 7 shape parameters, and (b) with 8 control points and 11 shape parameters. The control points and curves are indicated by dots (•) and dashed lines (--), respectively.

The approximate Bézier airfoil shapes shown in Fig. 5 are found by minimizing the norm of the difference between the actual RAE2822 shape and the curve shapes generated by Eq. 8. Adding more control points clearly yields a better approximation to the given airfoil shape. This will also translate to an improved control of the airfoil shape during optimization. However, with the additional control points comes additional computational cost, which is exactly the subject of this work.

4. Computational Fluid Dynamic Modeling

A single CFD simulation consists, in general, of four steps: the geometry generation, meshing of the solution domain, numerical solution of the governing fluid flow equations, and post-processing of the flow results, which involves, in the case of numerical optimization, calculating the objectives and constraints. In this section we present the high- and low-fidelity CFD models, as well as the calculation of the aerodynamic forces.

4.1. High-Fidelity Model

The flow is assumed to be steady, inviscid, and adiabatic with no body forces. The compressible Euler equations are taken to be the governing fluid flow equations. The solution domain boundaries are placed at 25 chord lengths in front of the airfoil, 50 chord lengths behind it, and 25 chord lengths above and below it. The computational meshes are of structured curvilinear body-fitted C-topology with elements clustering around the airfoil and growing in size with distance from the airfoil surface. The computer code ICEM CFD [14] is used for the mesh generation. The free-stream Mach number, static pressure, and angle of attack are prescribed at the farfield boundary.

Numerical fluid flow simulations are performed using the computer code FLUENT [15]. The flow solver is of implicit density-based formulation and the inviscid fluxes are calculated by an upwind-biased second-order spatially accurate Roe flux scheme. Asymptotic convergence to a steady state solution is obtained for each case. The iterative convergence of each solution is examined by monitoring the overall residual, which is the sum (over all the cells in the computational domain) of the L^2 norm of all the governing equations solved in each cell. In addition to this, the lift and drag forces (defined in Section 4.3) are monitored for convergence. The solution convergence criterion for the high-fidelity model is the one that occurs first of the following: a maximum residual of 10^{-6}, or a maximum number of iterations of 1000.

A grid convergence study was performed using the NACA 0012 airfoil at Mach number $M_\infty = 0.75$ and angle of attack $\alpha = 1°$. The study, shown in Fig. 6a, revealed that 407,676 mesh cells are needed for mesh convergence, and that particular mesh was used for the high-fidelity model. The overall simulation time for the case considered is around 67 minutes (Fig. 6b). The flow solver reached a converged solution after 352 iterations. The other meshes required around 350 to 500 iterations to converge, except the coarsest mesh, which terminated after 1000 iterations, with the overall simulation time around 9.5 minutes.

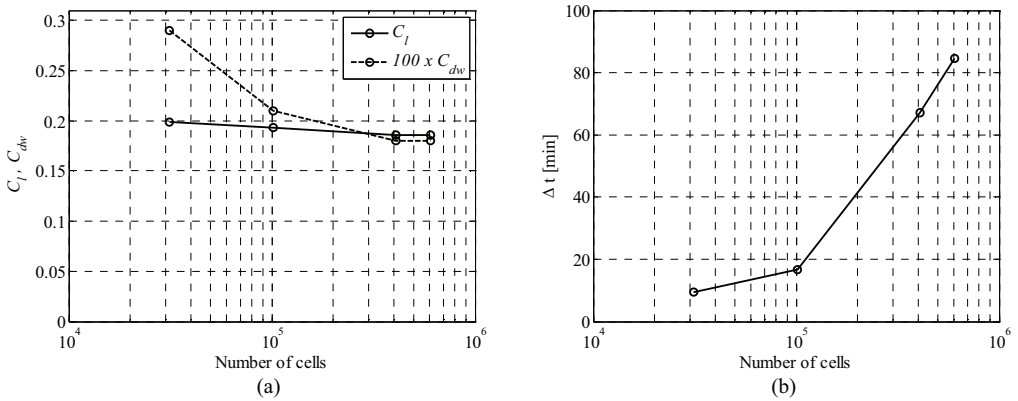

Fig. 6. Grid convergence study using the NACA 0012 airfoil at Mach number $M_\infty = 0.75$ and angle of attack $\alpha = 1°$; (a) lift and drag coefficients versus the number mesh cells, and (b) the simulation time versus the number of mesh cells.

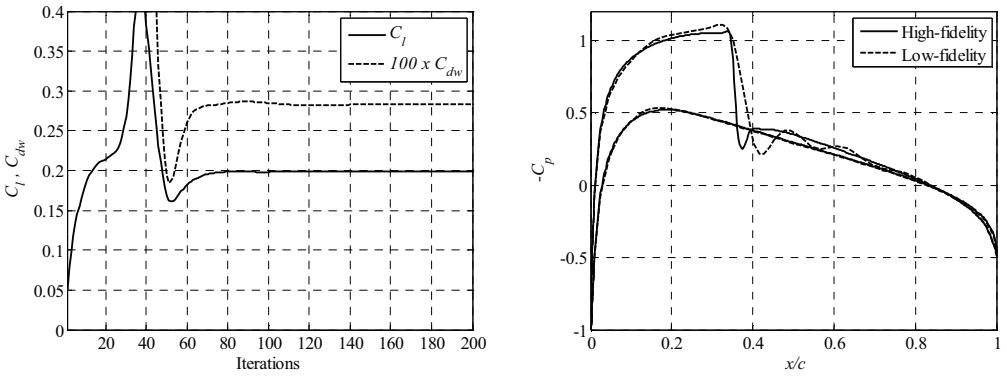

Fig. 7. Simulation results for NACA 0012 at Mach number M_∞ = 0.75 and angle of attack α = 1°; (a) evolution of the lift and drag coefficients obtained by the low-fidelity model; (b) comparison of the pressure distributions obtained by the high- and low-fidelity models.

4.2. Low-Fidelity Model

The low-fidelity CFD model is constructed in the same way as the high-fidelity model, but with a coarser computational mesh and relaxed convergence criteria. For the low-fidelity model, we use the coarse mesh in the grid study presented in Fig. 6a, with 31,356 mesh cells. The flow solution history for the low-fidelity model, shown in Fig. 7a, indicates that the lift and drag coefficients are nearly converged after 80 to 100 iterations. The maximum number of iterations is set to 100 for the low-fidelity model. This reduced the overall simulation time to 1.5 minutes. A comparison of the pressure distributions, shown in Fig. 7b, indicates that the low-fidelity model, in spite of being based on much coarser mesh and reduced flow solver iterations, captures the main features of the high-fidelity model pressure distribution quite well. The biggest discrepancy in the distributions is around the shock on the upper surface, leading to an over estimation of both lift and drag (Fig. 6a).

The ratio of simulation times of the high- and low-fidelity model in this case study is 43.8. In many cases the solver does not fully converge with respect to the residuals and goes on up to 1000 iterations. Then, the overall evaluation time of the high-fidelity model goes up to 170 minutes. In those cases the ratio of simulation times of the high- and low-fidelity models is around 110. For the sake of simplicity, we will use a fixed value of 80 in the numerical computations presented later in the paper.

4.3. Aerodynamic Forces

The aerodynamic forces are calculated by integrating the pressure distribution over the surface of the airfoil. The lift coefficient and the wave drag coefficient are calculated as

$$C_l = -C_x \sin\alpha + C_z \cos\alpha \ , \ C_{dw} = C_x \cos\alpha + C_z \sin\alpha \ , \tag{11}$$

where C_x and C_z are the horizontal and normal force coefficients, respectively, and are calculated by integrating the pressure distribution counter-clockwise around the surface of the airfoil as

$$C_x = \oint C_p \sin\theta \, ds \ , \ C_z = -\oint C_p \cos\theta \, ds \, , \tag{12}$$

where ds is the panel length on the surface of the airfoil and θ is the angle the panel makes with the horizontal-axis.

5. Numerical Study

The objective of this numerical study is to investigate the scaling properties of multi-fidelity shape optimization. We consider airfoil lift maximization at transonic flow conditions. In this section, we describe the general setup of the case study and discuss the results.

5.1. General Setup

The multi-fidelity optimization method described in Section 2 is utilized. The details of the problem formulation and the optimization algorithm are given in Sections 2.1 and 2.2, respectively. The surrogate model optimization is performed using a pattern-search algorithm [16], which is a derivative-free method. The high-fidelity CFD model is described in Section 4.1 and the low-fidelity CFD model in Section 4.2. The surrogate models are constructed using the SPRP technique, described in Section 2.3.

Three optimization runs were performed with the airfoil shape described by 3, 7, and 11 design variables. The NACA 4-digit parameterization (Section 3.1) is used for the 3 design variable case, and Bézier curves (Section 3.2) are used in the other two. To ensure that realistic airfoil sections are obtained with the Bézier curve parameterization, additional nonlinear constraints are implemented to ensure that the upper and lower surfaces do not cross, and that the chordwise values of the free control points on the upper and lower surfaces are monotonic.

The transonic design case considered in this study has a free-stream Mach number $M_\infty = 0.75$ and angle of attack $\alpha = 1°$. The objective is to maximize the lift coefficient C_l, with constraints on the wave drag coefficient, $C_{dw.max} = 0.0060$, and on the non-dimensional cross-sectional area, $A_{min} = 0.075$. The initial designs in all design cases are approximations to the RAE2822 airfoil shape. These approximation shapes are obtained for each design case by minimizing the norm of the difference between the RAE2822 and the airfoil shape obtained by the parameterization. The initial designs are slightly different in each case, since number of design variables differ.

5.2. Results

The initial airfoil shapes are shown in Fig. 8a. Although all initial airfoil shapes are an approximation to the same airfoil shape, RAE2822, there is a difference between them due to different number of design variables. As a result, the lift and drag coefficients vary considerably for the initial designs (Table 1). In spite of this, the optimizer is able converge to similar designs (Fig. 8b), each with the same value of the drag coefficient (Table 1). The only notable difference is at the trailing-edge, where the additional control points provide an extra capability to modify the shape. As a result, the optimized airfoil in Case 3 (with 11 DV's) has the largest lift, when compared to the other cases (the 3 and 7 DV cases).

The computational cost increases with additional design variables (Table 1). From Case 1 to Case 2, the number of high-fidelity iterations increases by 3 (4 to 7), and from Case 2 to Case 3 by 2 (7 to 9). The number of iterations of the surrogate model increases more rapidly. Case 1 needs 600 iterations and Case 2 1050, giving an increase of 450 iterations with the additional 4 DV's. The number of iterations increases to 2000 for Case 3, an increase of 950 for the additional 4 DV's. The overall computational cost rises accordingly. Expressed in the number of equivalent high-fidelity iterations, the cost is less than 12 for Case 1, less than 21 for Case 2, and 34 for Case 3. Figure 8c shows the variation in the computational cost. Thus, the design optimization cost increases more or less linearly in terms of the number of algorithm iterations. The worse-than-linear increase of the overall cost is mostly due to the surrogate model optimization, indicating that further reduction of the optimization cost can be obtained by improving efficiency of this particular step of the design process.

Table 1. Numerical results for the three airfoil design optimization cases with 3, 7, and 11 design variables (DVs). N_c is the number of low-fidelity model evaluations and N_f is the number of high-fidelity model evaluations. All the numerical values are from the high-fidelity model.

	Case 1 (3 DVs)		Case 2 (7 DVs)		Case 3 (11 DVs)	
Variable	Initial	Optimized[#]	Initial	Optimized[#]	Initial	Optimized[#]
C_l	0.5978	0.4654	0.3218	0.6415	0.7850	0.7684
C_{dw}	0.0104	0.0060	0.0011	0.0060	0.0128	0.0060
A	0.0774	0.0761	0.0792	0.0854	0.0778	0.0756
N_c	–	600	–	1050	–	2000
N_f	–	4	–	7	–	9
Total cost[*]	–	< 12	–	< 21	–	34

[#] Design obtained using the algorithm described in Section 2; surrogate model optimization performed using the pattern-search algorithm [16].
[*] The total optimization cost is expressed in terms of the equivalent number of high-fidelity model evaluations. The ratio of the high-fidelity model evaluation time to the corrected low-fidelity model evaluation time varies between 43.8 to 110 depending on the design. For the sake of simplicity we use a fixed value of 80 here.

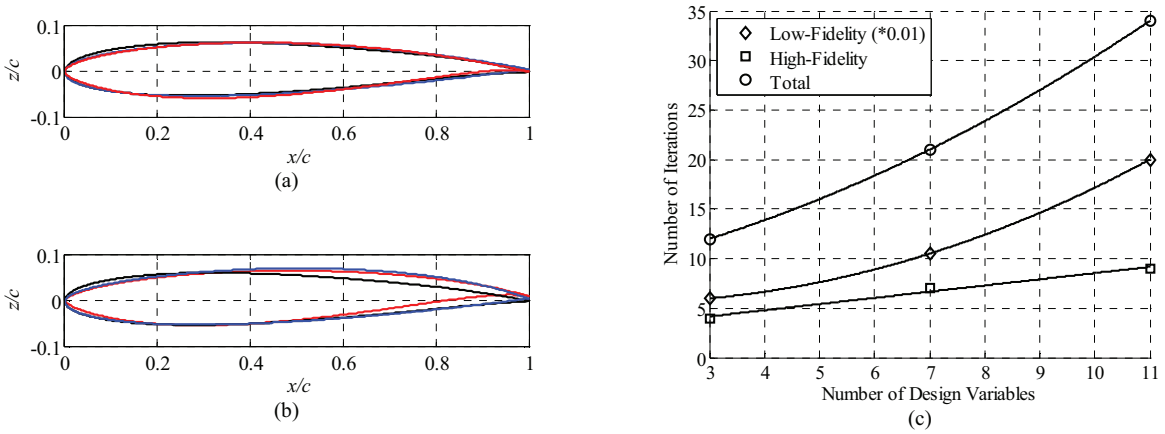

Fig. 8. Results of the numerical optimization: (a) initial airfoil shapes (Case 1: black, Case 2: blue, Case 3: red); (b) optimized airfoil shapes (Case 1: black, Case 2: blue, Case 3: red); (c) variation of the computational cost with the size of the design space for the three cases, shown are the cost of the low-fidelity (diamonds), high-fidelity (boxes), and the total cost (circles).

6. Conclusions

We have investigated the scaling properties of a multi-fidelity shape optimization algorithm. The relationship between the dimensionality of the design space and the computational cost of the airfoil shape optimization was observed. Although these results can only be considered as preliminary and further case studies need to be carried out, it seems that the design cost scales at most linearly with respect of the number of high-fidelity model evaluations. The overall optimization cost increases faster, which is due to the computational overhead related to the surrogate model optimization. This indicates that the construction and the optimization of the surrogate model needs to be addressed. In particular, when using coarser mesh resolution CFD models, the necessary mesh density needs to be investigated. Moreover, the optimization technique needs to be able to handle the numerical noise in the low-fidelity model.

References

1. Queipo, N.V., Haftka, R.T., Shyy, W., Goel, T., Vaidyanathan, R., and Tucker, P.K., "Surrogate-Based Analysis and Optimization," *Progress in Aerospace Sciences*, Vol. 41, No. 1, 2005, pp. 1-28.
2. Forrester, A.I.J., and Keane, A.J., "Recent advances in surrogate-based optimization," *Progress in Aerospace Sciences*, Vol. 45, No. 1-3, 2009, pp. 50-79.
3. Koziel, S., Echeverría-Ciaurri, D., and Leifsson, L., "Surrogate-based methods," in S. Koziel and X.S. Yang (Eds.) *Computational Optimization, Methods and Algorithms*, Series: Studies in Computational Intelligence, Springer-Verlag, pp. 33-60, 2011.
4. Alexandrov, N.M., Lewis, R.M., Gumbert, C.R., Green, L.L., and Newman, P.A., "Optimization with Variable-Fidelity Models Applied to Wing Design," *38th Aerospace Sciences Meeting & Exhibit*, Reno, NV, AIAA Paper 2000-0841, Jan. 2000.
5. Barrett, T.R., Bressloff, N.W., and Keane, A.J., "Airfoil Design and Optimization Using Multi-Fidelity Analysis and Embedded Inverse Design," AIAA Paper 2006-1820, *47th AIAA/ASME/ASCE/AHS/ASC Structures, Structural Dynamics, and Materials Conference*, Newport, Rhode Island, 2006.
6. Leifsson, L., and Koziel, S., "Multi-fidelity design optimization of transonic airfoils using physics-based surrogate modeling and shape-preserving response prediction," *Journal of Computational Science*, Vol. 1, No. 2, 2010, pp.98-106.
7. Nelson, A., Alonso, J.J., Pulliam, T.H., "Multi-Fidelity Aerodynamic Optimization using Treed Meta-Models," *25th AIAA Applied Aerodynamics Conference*, Miami, FL, June 25-28, 2007.
8. Viswanath, A., Forrester, A.I.J., and Keane, A.J., "Dimension Reduction for Aerodynamic Design Optimization," *AIAA Journa*l, vol. 49, no. 6, 2011, pp.1256-1266.
9. Bandler, J.W., Cheng, Q.S., Dakroury, S.A., Mohamed, A.S., Bakr, M.H., Madsen, K., and Sondergaard, J., "Space mapping: the state of the art," *IEEE Trans. Microwave Theory Tech.*, vol. 52, no. 1, pp. 337-361, Jan. 2004.
10. Koziel, S., Cheng, Q.S., and Bandler, J.W., "Space mapping," *IEEE Microwave Magazine*, vol. 9, no. 6, 2008, pp. 105-122.
11. Koziel, S., "Shape-preserving response prediction for microwave design optimization," *IEEE Trans. Microwave Theory and Tech.*, vol. 58, 2008, pp. 2829-2837.
12. Abbott, I.H., and Von Doenhoff, A.E., *Theory of Wing Sections*, Dover Publications, 1959.
13. Lepine, J., Guibault, F., Trepanier, J.-Y., and Pepin, F., "Optimized Nonuniform Rational B-Spline Geometrical Representation for Aerodynamic Design of Wings," *AIAA Journal*, Vol. 39, No. 11, 2001, pp. 2033-2041.
14. ICEM CFD, ver. 13, ANSYS Inc., Southpointe, 275 Technology Drive, Canonsburg, PA 15317, 2011.
15. FLUENT, ver. 13, ANSYS Inc., Southpointe, 275 Technology Drive, Canonsburg, PA 15317, 2011.
16. Koziel, S., "Multi-fidelity multi-grid design optimization of planar microwave structures with Sonnet," *International Review of Progress in Applied Computational Electromagnetics*, Tampere, Finland, 2010, pp. 719-724.